High-frequency breakdown in dynamic tunable-barrier quantum dots

Nathan Johnson,[*,†] Gento Yamahata, and Akira Fujiwara[‡]
NTT Basic Research Laboratories, NTT Corporation, 3-1 Morinosato Wakamiya, Atsugi, Kanagawa 243-0198, Japan

(Received 30 September 2025; accepted 18 November 2025; published 17 December 2025)

Tunable-barrier dynamic quantum dots are known to generate very accurate single-electron-based currents and can be used as a source of single-electron wave packets for use in quantum metrology, sensing, or information processing. To realize their full technological potential, it is desirable to maximize their frequency of operation to increase the current; however, it has been observed that the mechanism of electron transfer across the quantum dot consistently breaks down for gigahertz frequencies, and this remains unexplained. Here, we present an analysis technique, combined with detailed modeling, to present a mechanism of high-frequency breakdown in this class of quantum dots as a rapidly imparted momentum impulse. Such understanding aids future design and operation protocols, allowing their use in high-frequency and real-time quantum measurements and technologies.

DOI: 10.1103/1mtz-rkqp

Quantum dots (QDs) have traditionally found widespread use in studies of electron transport in condensed matter physics [1–3], with many of these studies having focused on using dc or low-frequency transport. Recently, there have been proposals to use QDs as high-accuracy current sources, or as fast sensing devices [1,4]. In these proposals, the QD is either used as a source of high-fidelity wave packets [5–8] or as a tool itself to study fast quantum-coherent events such as excitation or entanglement [9–11]. In both classes of experiment, the QD is used dynamically, with its energy with respect to the leads or its confinement being changed in time to favor electron capture, ejection, select specific states, or preserve coherence. To achieve this, it is desirable to move to high-frequency operation (of the order of gigahertz), either to increase the number of wave packets created for ease of measurement [5,12,13] or to sample coherent phenomena [9,14,15]. Further, a high-frequency QD can aid the realization of quantum computing architectures that use coherent QD states [16–18], or serve as high-frequency qubit structures and linkages [19–21].

The state-of-the-art QD architectures employed in such applications use an electrostatically defined and dynamically controlled QD embedded in a semiconductor heterostructure, and they are commonly referred to as tunable-barrier QDs [1]. The QD is defined by time-varying electrostatic tunnel barriers that permit electron transport into and out of the QD in specified time windows, enabling a clock-controlled charge-transfer process. In the above applications, charge may be transferred in a single, one-off process, or continuously as a stream of individual wave packets that form a dc current. In the present study, we will focus on the breakdown of the dc current in the high-frequency regime, and we will show that the mechanism of this breakdown is based on electrostatically driven single-electron transfer events, which can be explained by a simple model considering the electron dynamics inside a QD.

The accuracy of a QD as discussed here refers to its ability to transfer a precisely defined number of charges per clock cycle. This accuracy of charge transfer, and hence its usability in technological applications, depends on several factors. The detailed mechanism of the electron transfer across the QD in this class of electrostatic dynamic quantum dots is well understood in the adiabatic limit, when the transfer process occurs with the electron remaining in the QD ground state, and is described by the decay-cascade model [22]. This model describes the electron loading and isolation process, and it has been well verified experimentally in several materials, including the most accurate state-of-the-art tunable-barrier QDs in silicon and GaAs. Empirically, the adiabatic limit is found to be approximately 1 GHz in this important class of dynamic QD, where the decay-cascade model is found to begin to break down.

The principal limitation of high-frequency operation in QDs arises from the nonadiabatic (NA) excitation [12,23]. This generic term describes processes that cause unwanted

*Contact author: nathan.johnson@ucl.ac.uk
†Present address: London Centre for Nanotechnology, University College London, 17–19 Gordon Street, London WC1H 0AH, United Kingdom.
‡Contact author: akira.fujiwara@ntt.com

excitation to a resident electron, which allows a greater chance of escape from the QD, and so the electron-capture process fails and hence the accuracy of transfer decreases. This term describes an electrostatically induced excitation, which can be to a population of higher-energy states, depending on the confinement and level structure of the QD. In addition, the coherence may be reduced. This reduction in accuracy has been shown to be detrimental for the above applications [1,24]. Typically, the generated charge transfer from source to drain, i.e., the dc current, deviates from that predicted by the adiabatic decay-cascade model and declines to zero at high frequencies. While this NA-induced breakdown was observed in many electrostatically defined architectures, like its adiabatic counterpart—demonstrating the material independence and electric origins of the effect—the exact mechanism of the breakdown remains largely unknown. Here, we begin to clarify this by detailing a mechanism of this breakdown. This effort can influence future gated semiconductor designs and measurement protocols and allow the realization of high-frequency quantum measurements and wave-packet sources. We present data and a model that extends the decay-cascade model into the nonadiabatic regime.

In this work, we use an analysis technique based only on the dc throughput current and develop a model that reveals the NA excitation to be a sharp momentum transfer imparted to an electron resident in the QD. In our study, we use a gate-defined silicon QD and operate it dynamically [12,25–27], such that a well-defined number of electrons can be loaded into the QD and expelled with a recurring frequency f. Our system is analogous to those constructed in other semiconductor media [1,24]. We use the decay-cascade model as a basis of our study of the NA excitation [22]. In the NA case, some electrons are excited during the loading of the dynamic QD, which will induce a further electron escape back to the source. In our work, we use a higher-energy (HE) state to sample these NA-excited electrons. The HE state could be either a trap state [9,28,29] or an intrinsic excited state of the QD. We note that this HE state is sampling the NA-induced excitations, and that other excitations may also arise and contribute to the breakdown of the dc current. In addition, our method provides a complementary technique to study the phonon coupling to a resident electron, as we also account for thermal activation of the HE state. We derive a model that can recreate the thermal and NA components of the excitation with considerable accuracy and find that the NA-excitation can only be understood as a sudden impulse on the electron, whereas the thermal excitation can be separated as a lattice phonon interaction as expected. Our analysis technique of deriving excitation rates from dc current could prove useful in understanding and constructing future quantum measurements and enhance sensing protocols, in addition to the knowledge gained on the origin of the excitation itself.

I. MEASUREMENT OF NONADIABATIC EXCITATION

A sketch of the device used is shown in Fig. 1(a). The QD, shaded in blue, is formed electrostatically between two polycrystalline-Si gates G_1 and G_2, separated by 100 nm, that lie above a Si nanowire [30]. An additional upper gate covers the area in the sketch to aid conduction. The QD is formed when we apply the potentials V_{G1} and V_{G2} to gates G_1 and G_2, respectively. We operate the QD dynamically, in a similar way to single-electron current sources [1,26]. The potential V_{G1} is driven periodically by a sinusoidal waveform $V_{G1}^{ac}(t)$ with period $1/f$, while V_{G2} is held constant. During a single period of $V_{G1}^{ac}(t)$, the potential underneath G_1 drops below the Fermi energy, allowing electrons from the source to populate the QD region. As the potential rises, the QD is formed and electrons are isolated within it. As the potential continues to rise, the QD potential rises above that of V_{G2}, and the resident electrons are ejected to the drain. This forms a dc current $I_d = nef$, where n is the captured population of the QD and e is the electronic charge. This process is denoted with black arrows in Fig. 1(a). We develop our analysis using only a straightforward measurement of I_d. The previously introduced decay-cascade model provides a master-equation-based formalism to describe this process.

Because the ejection process from the QD can be made to occur with unit probability, I_d is a measure of the capture dynamics, and hence this capture stage determines the effectiveness of the QD to act as a current source or of coherent wave packets. This electrostatic scheme is material independent [1,24] and allows us to measure the generic incoming process to a QD driven in this way. The accuracy of this process can be evaluated by comparing I_d to the expected current nef, within the resolution of the measurement noise. The sample is mounted in a temperature-controllable dilution refrigerator in zero magnetic field.

In our device, we also observe the presence of an HE state, which is known to sometimes occur in silicon devices [9,28]. We speculate that this state could be an instance of two possibilities: it could be an intrinsic excited state of the QD, or it could be a (trap) state of a parasitic QD in parallel to the main QD, as depicted in Fig. 1(a). In the case of the HE state being attributable to a trap-like QD, we find in our case its ground-state energy is at a higher potential than that of the main QD, as we do not see parallel current flow across the QD system. The HE state serves to return electrons to the source lead, depicted with arrows in Fig. 1(a), as we will show later. The breakdown in accuracy seen with NA excitation is attributed entirely

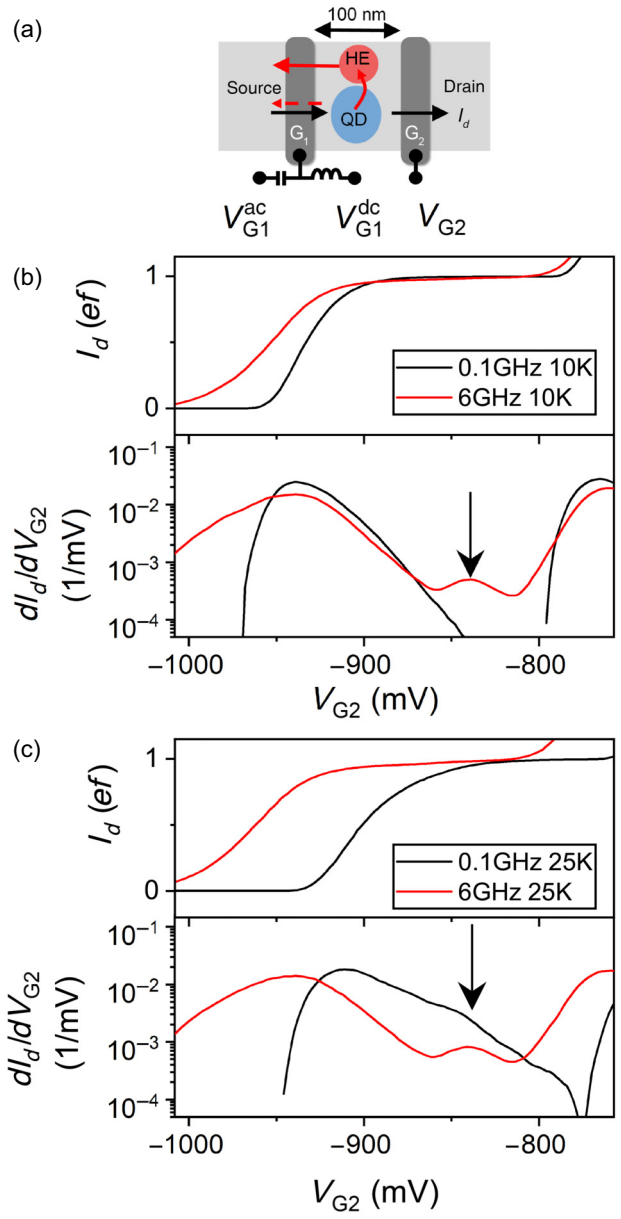

FIG. 1. (a) Schematic of the device used in this work. The main QD is shaded in blue, and the HE state is shown in red. Arrows denote the possible electron paths: black, capture and forward escape, defining I_d; red solid, escape to source via the HE state; red dash, direct escape to source. (b),(c) Upper panel: the QD current I_d shows a clear plateau reflecting the capture process. Lower panel: the derivative dI_d/dV_{G2} shows the captured-electron distribution. Black trace, 0.1 GHz, adiabatic capture; red, 6 GHz, NA excitation present. Arrow highlights the distribution formed from the HE-state population. At 10 K, (b) shows no HE state component at 0.1 GHz, but in (c) at 25 K, we see thermal activation to the HE state can occur.

to current returning to the source during the capture stage of the driving, though we note that there are likely other states, in addition to the HE state, through which this can occur.

In Figs. 1(b) and 1(c), we show the current I_d (upper panel) and the derivative dI_d/dV_{G2} (lower panel). As V_{G2} is varied from higher potential (more negative voltage) to lower, plateaus of current are seen in I_d for successive n. In this study, we restrict ourselves to the first plateau, where $n = 1$, which corresponds to ejection of a single electron from the QD and is of greatest interest in most applications; however, our analysis extends to multiple n due to the nature of charge transfer and excitation being based on sequential single-electron processes [22]. We use a frequency f of 0.1 GHz as a basis for adiabatic transfer through the QD, plotted in black in Figs. 1(b) and 1(c). At this frequency, electron transport across the QD occurs adiabatically [1,22,31] and the decay-cascade model has been verified [22,32–34]. In our device, we also confirm the accuracy of this model for I_d at $f = 0.1$ GHz. We use this confirmation as a basis to verify that I_d measured at $f = 0.1$ GHz is entirely developed from adiabatic (ground-state) capture to the QD. We will use this adiabatic dataset as a basis to compare the ground- and excited-state cases.

The derivative dI_d/dV_{G2} shows a well-defined characteristic distribution reflecting the decay-cascade model conforming capture statistics, and this is plotted in Fig. 1(b) (lower panel, black trace). By contrast, we plot the equivalent trace at $f = 6$ GHz in red. Here, we see that this distribution is broadened, which we attribute to the high-frequency NA breakdown in the capture process, and hence the accuracy of I_d is reduced. More importantly, as highlighted with an arrow in Fig. 1(b), we see a separate distribution, which we attribute to electrons being promoted to the HE state by the NA excitation, and returning to source [see Fig. 1(a)] [23]. This HE-state distribution puts a limit on the accuracy because it degrades the flatness of the current plateau, as it is sampling a proportion of QD electrons that probabilistically undergo the NA-excitation process. The HE-state distribution is equivalent to a population of excited electrons. By studying this distribution under varying frequency and temperature (which principally drive the NA and phononic components, respectively), we can derive a model of the NA excitation process. Note that at 6 GHz, we see an anomalously slow riser around the onset of the pump current, which could be because the height of the entrance barrier [30] is too low in this regime, and we move outside the validity of the decay-cascade model.

In Fig. 1(b), the traces are recorded at a temperature of $T = 10$ K, which is sufficiently low to maintain ground-state capture, and thermal fluctuations are negligible [30,34,35].

In Fig. 1(c), we plot the equivalent measurements of I_d but at $T = 25$ K. We see at this elevated temperature that the HE state can be populated by the thermal activation at low f (lower panel, black, highlighted). At high f, there is an increase in amplitude of the HE-state population. As with NA excitation, this thermal escape to the source

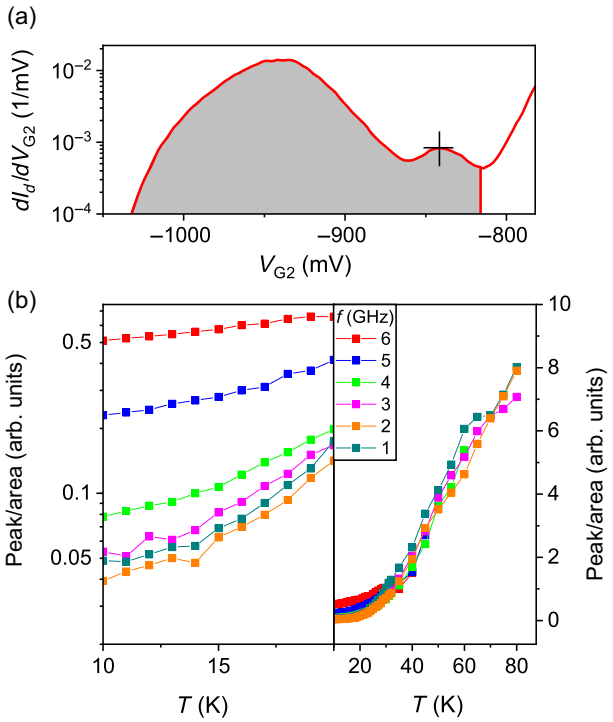

FIG. 2. (a) Example of the quantitative sampling peak-to-area method. The peak is marked with a cross, and the shaded area denotes the captured population. (b) The peak-to-area measure of the HE-state population. Left panel: for $f = 1$–6 GHz we see a progression in the ratio attributable to NA excitation. Right panel: temperature evolution at all frequencies.

can also be direct from the main QD. Both the NA excitation and thermal energy produce similar effects on the distributions but from different origins. We will account for the electron-phonon coupling during this capture phase in addition to the NA excitation. As we see in Fig. 1(c), the HE state can sample this excitation by capturing these higher-energy electrons from both NA and thermal origin.

To quantify these effects, we measure I_d over 0.1–6 GHz to see the progression of the NA breakdown, and over a temperature range $T = 10$–80 K to see the thermal effect. We find that, even in the high-f case, where the HE state has the highest occupation, the current lost via excitation to the HE state and relaxation to the source is of the order of picoamps, making it difficult to evaluate quantitatively.

Therefore, we analyze the HE-state population as shown in Fig. 2(a). Here, we show a sample derivative trace dI_d/dV_{G2} (red), similar to those of Figs. 1(b) and 1(c). The shaded area corresponds to the captured electron distribution and is thus a measure of the actual I_d, including inaccuracy. We note the similarity in shapes of the main QD and HE-state distributions. The shape is largely determined by the cross-coupling between the QD and G_1. Hence, the similarity between the distribution shapes allows us to infer that the cross-coupling between the HE state and G_1 is quite similar. We see that $I_d < 1$ over this region always, which confirms that the HE state is not contributing electrons to the main QD, and thus we show that the loading process largely follows the adiabatic decay-cascade model. This allows us to assume that the HE-state distribution is monotonic with population. As the frequency of operation increases, we observe the decrease in the total pumped current, given by the shaded area of Fig. 2(a). We attribute this decrease to the NA process. The HE state samples some of these electrons that undergo the NA process. With the small size of the distribution, we can take the peak height as a less noisy measure than the HE-state peak area, as marked with a cross on Fig. 2(a). To normalize the HE-state distribution to the total pumped current, we consider the shaded area to be the actual pumped current I_d, as opposed to the ideal value of nef. This is because, as we increase the frequency and temperature of the device, we observe a broadening of the main distribution due to non-decay cascade tunneling (and not via the HE state) from the QD, and so our method accounts for this reduction in total pumped current.

In Fig. 2(b) we plot this peak-to-area ratio. In the left-hand panel, we can see a clear frequency dependence, with higher f showing a larger HE-state population, attributable to the NA excitation. In the right-hand panel, we can see a clear T dependence, as the HE state is thermally populated, universally at all frequencies. To understand how the HE state can be populated due to the NA process captured in the analysis in Fig. 2, we will use both the temperature and frequency dependence of the HE-state current.

II. MODEL

To separate the thermal and NA components, we derive a model as sketched in Fig. 3(a). We construct a two-level system consisting of the QD ground state $U_G(t)$ and the HE state $U_E(t)$. Due to the similar coupling between each state and G_1, the two states can be separated by a fixed energy E. These two levels are used to represent the total spectrum of states available to an electron in the QD and HE state, respectively. The barrier top, denoted by $U^{ac}_{G1}(t)$, rises with $V^{ac}_{G1}(t)$; $U_G(t)$ and $U_E(t)$ also rise together but at some slower rate determined by the cross-coupling between the gate and the QD and HE-state system [9,30]. The arrows in Fig. 3 denote the allowed transitions: the black arrows show escape to the source, the red arrows denote thermal excitation and relaxation, and the blue arrow shows the NA excitation.

The time evolution of the total population of the QD and HE-state system is [14]

$$\frac{\mathrm{d}P_G(E,t)}{\mathrm{d}t} = -\Gamma_{\uparrow}P_G(E,t) + \Gamma_{\downarrow}P_E(E,t) - \Gamma_G P_G(E,t)\left(1 - F\left(U_G(t)\right)\right)T_G(E), \quad (1)$$

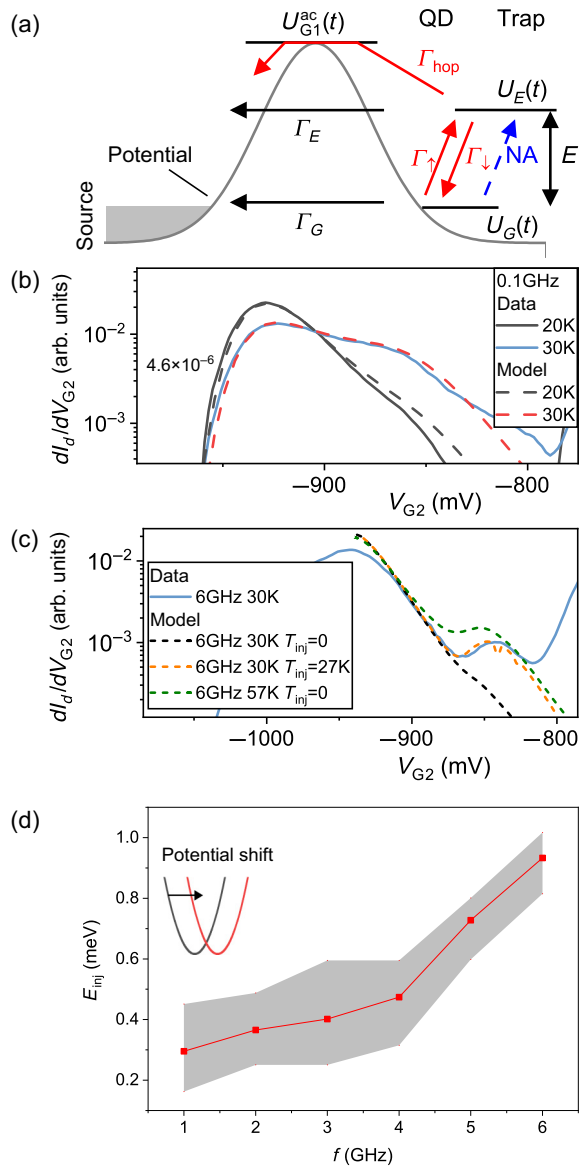

FIG. 3. (a) Schematic of the model. Arrows denote the allowed transitions, labeled by the attempt frequency of the transition. The terms in Eqs. (1) and (2) in the main text describe the rates of each transition. (b) Determination of the pair (Γ_{ph}, E) by mapping to 0.1 GHz (adiabatic) data finds $(1 \times 10^{11}\ s^{-1}$, 9 meV). (c) Verification of the shape of the HE-state distribution. A nonzero E_{inj} is required to get the peak shape of the NA distribution, whereas using an increased (lattice-temperature) T gives the more rounded shape, as also seen in (b). (d) Injected energy E_{inj} as a function of frequency f. The shaded region shows the variability in the range $T = 20$–30 K. The sketch highlights the dominant component of E_{inj} as a potential shift.

$$\frac{dP_E(E,t)}{dt} = \Gamma_\uparrow P_G(E,t) - \Gamma_\downarrow P_E(E,t) - \Gamma_E P_E(E,t)\,(1 - F\,(U_E(t))\,T^{th}_E(E) - \Gamma_{hop} P_E(E,t)\left(1 - F\left(U^{ac}_{G1}(t)\right)\right) T^{th}_E(E), \quad (2)$$

where $P_{G,E}(E,t)$ denotes the population P of the state $U_{G,E}(t)$. Each of the arrows depicting allowed transitions in Fig. 3(a) is labeled by the corresponding attempt frequency.

Thermal interactions are expressed as $\Gamma_\uparrow = \Gamma_{ph}\exp(-E/kT)$ and $\Gamma_\downarrow = \Gamma_{ph}$ and follow the detailed balance, and Γ_{hop} is a thermal-escape rate. Further, $\Gamma_{G,E}$ is an attempt frequency from each state, and we take $\Gamma_G = \Gamma_E$; $F(\epsilon)$ is the Fermi function and $T_{G,E}(E)$ is a transmission coefficient (see the Appendix for a full description of the model terms) [30]. In addition, $U_G(0) \equiv -E_c$, where E_c is the charging energy and $U^{ac}_{G1}(0)$ varies proportionally to V_{G2} [30]; k is Boltzmann's constant; and T_0 is a constant. This evolution allows only for direct (tunneling) escape from the QD and HE state and thermal activation of the HE state [see also Fig. 1(a)]. Note that we use $\Gamma_{hop} = \Gamma_{ph}$ for the thermal activation from the HE state for simplicity because the corresponding barrier height is low enough. We simultaneously solve the master equations (1) and (2) for varying $U^{ac}_{G1} \propto V_{G2}$ to form a current equivalent to those measured in Figs. 1 and 2.

Figure 3(b) plots two traces at 0.1 GHz at a low (20 K) and high (30 K) temperature. The data show that the HE state is populated more significantly at 30 K. The dashed lines show the result of the above model, with no NA excitation included, where we have used $\Gamma_G = 10$ THz, $\Gamma_{ph} = 0.1$ THz, and $E = 9$ meV, chosen as a best fit to the data. We find that Γ_{ph} is in agreement with literature values [36].

We now incorporate the NA excitation into our model. In Fig. 3(b), the initial zero-time loading condition was a Fermi distribution shared between $U_G(0)$ and $U_E(0)$. This Fermi distribution gives the initial populations of $U_G(0)$ and $U_E(0)$ that we then use to solve the master equations (1) and (2). We introduce the NA excitation as a rapid impulse at $t = 0$—an electron in the QD receives a sudden momentum gain, which can cause the excitation. We define T_{inj} such that the zero-time Fermi distribution is calculated as an effective temperature $T_{start} = T + T_{inj}$. This zero-time distribution is used to calculate the populations at $U_G(0)$ and $U_E(0)$. Note that T_{start} is not a real temperature if NA excitation exists, which can place the QD into a nonequilibrium condition. In our model, we only modify the zero-time populations (see the Appendix for details) $P_{G,E}(0)$ by using T_{start}. Then, for all later times, the dynamics proceed using only the lattice temperature T. Figure 3(c) compares this model with data. We plot data for $f = 6$ GHz at 30 K. In the black dashed line, we show the model result using $T_{inj} = 0$, that is, $T_{start} = T = 30$ K, which shows a small HE-state population, but far less than the data. In orange, we see that we can match the data well if we choose $T_{inj} = 27$ K and run the model with $T_{start} = T + T_{inj} = 30 + 27$ K. By contrast, in green, we also plot the effect of $T_{inj} = 0$ but $T = 57$ K, so $T_{start} = T + T_{inj} = 57 + 0$ K (effect of continuous energy

injection), which clearly shows a different shape, similar to the low-frequency plots of Fig. 3(b). We see that the effect of a sudden impulse via $T_{\rm inj}$ is to produce a more rounded, well-defined distribution, while continual thermal activation results in a flatter shape, and within the context of the two-level system model, supports the conclusion of a sudden momentum impulse. We suggest this gives strong evidence that the NA mechanism is of the form of a fast impulse rather than a continual energy injection, in agreement with a related study [9].

In the above model, $T_{\rm inj}$ is a fit parameter that is useful as a guide to compare the effect of lattice temperature and that of the NA excitation, as shown in Fig. 2(b); however, as noted above, it is an effective temperature and does not represent any physical quantity. To be more accurate, we define an injected energy $E_{\rm inj}$, which better quantifies the NA impulse as an energy injection. To be fully general and quantitative, we can assert $P_E^{\rm inj} = P_E(T + T_{\rm inj}, t = 0) - P_E(T, t = 0)$, where we are separating the proportion of the initial populations that we require to match the data from the thermal equilibrium case. Then $E_{\rm inj} = EP_E^{\rm inj}$, with $E = 9$ meV, as found earlier.

In Fig. 3(d), we plot $E_{\rm inj}$ for $f = 1$–6 GHz and $T = 20$–30 K in 1-K increments. This is done by inspection while running the model with various $T_{\rm inj}$. The red trace shows the mode of the values, and the shaded area shows the range of $E_{\rm inj}$, clearly supporting the data of Fig. 2(b).

III. DISCUSSION

We interpret $E_{\rm inj}$ as an excess kinetic energy imparted to the electron as the QD forms and is isolated from the source when $U_{\rm G1}^{\rm ac}(t)$ crosses the Fermi energy. We can attribute the main mechanism for this to the dynamic shift in the position of the QD, which results in velocity gain and spatial oscillation of the single-electron wave packet inside the QD [9]. There may be some smaller contribution from a changing QD confinement during the capture process.

For a potential shift, we suggest $E_{\rm inj} \equiv \frac{1}{2}mv^2$, where m is the reduced mass and v is the excess speed of the wave packet. For the range $f = 1$–6 GHz, we find $v = 20$–40 nm/ps, which is aligned with a previous estimate [9]. We can roughly deduce that the QD center shifts by $x \sim 26$–44 nm during the NA impulse, which is plausible with the 100-nm lithographic separation of the gates [9]. We expect $v \propto f$ and thus $E_{\rm inj} \propto f^2$, which we see some evidence of in Fig. 3(d). We note that in the limit where the QD shape remains harmonic throughout the NA process, we would expect the excitation to result in only a slightly perturbed Fermi distribution, thus reinforcing the $E_{\rm inj}$ found here, although we note the caveat regarding the reliability of $T_{\rm inj}$ as a measure of a real temperature.

Although in general there can be another type of NA excitation from confinement-shape change, our recent results using a QD device simulator [37] suggest that the effect would be minor because the confinement change is small and rather symmetric. Furthermore, the QD confinement is likely pinned by impurities and barrier-potential fluctuations in the channel, which have a weaker capacitive coupling to $V_{\rm G1}^{\rm ac}(t)$. In agreement with a previous study [9], we suggest the origin of NA excitation in this case to be largely dominated by a sudden potential shift.

In conclusion, we have shown an analysis technique that uses only the dc throughput current of a QD to allow us to estimate the phonon coupling and NA components and provide some insight into the time dependence of the QD potential profile. While high-frequency breakdown was often observed, direct quantitative study of its mechanism had previously been elusive. Our method could also be adapted to provide quantum sensing of the electron wave function or to track dynamic changes in electric field. We have provided a quantitative study of the mechanism of NA breakdown in QDs and shown evidence supporting the QD position shift as a dominant component in the high-frequency breakdown. We find that this result complements and extends the adiabatic decay-cascade model into the high-frequency nonadiabatic regime. By comparing the HE-state population under the influence of thermal activation and frequency-related momentum transfer, we can differentiate the continuous thermal component and distinguish it from the sudden NA component. While we have built our results on the decay-cascade model because it was applicable to our device in the adiabatic limit, we suggest that our conclusion is more general and may hold for other classes of QD operation. To overcome the breakdown, we recommend the use of a plunger gate over the QD, which can allow finer control of the QD profile and decouple it from the ac potential oscillation. A split gate could be used as the loading gate G_1, which could help restrict the momentum transfer to the electron.

ACKNOWLEDGMENTS

This work was partly supported by JSPS KAKENHI Grant No. JP18H05258.

DATA AVAILABILITY

The data that support the findings of this article are available from the authors upon reasonable request.

APPENDIX: DERIVATION OF MODEL TERMS

Here, we describe the selection of the parameters included in the model used to derive the NA and thermal components in the main text. The derivation of this model and parameters largely follow discussions published in Refs. [9,30,35], and we only outline parameters here. The model is described by Eqs. (A4) and (A5) in the main text. We write the transmission coefficients used in these

equation as [30]

$$T_G = \frac{\exp(-(U^{ac}_{G1}(t) - U_G(t))/kT_0)}{1 + \exp(-(U^{ac}_{G1}(t) - U_G(t))/kT_0)}, \tag{A1}$$

$$T^{tn}_E = \frac{\exp(-(U^{ac}_{G1}(t) - U_E(t))/kT_0)}{1 + \exp(-(U^{ac}_{G1}(t) - U_E(t))/kT_0)}, \tag{A2}$$

$$T^{th}_E = \exp\left(\frac{-(U^{ac}_{G1}(t) - U_E(t))}{kT}\right). \tag{A3}$$

Here, we have divided the transmission coefficient into two terms, corresponding to tunneling and thermal activation respectively, and T_0 is a constant [30]. In the QD coefficient, T_G [Eq. (A6)], we neglect the thermal-activation term for simplicity, as it has little effect due to the QD having a lower potential than the HE state and the fast-rising barrier $U^{ac}_{G1}(t)$ [14,30]. We use the same transmission coefficients to describe the incoming terms [the reverse processes for each of the processes that allow escape to source; see Fig. 3(a)], which are included in the analytical model. These terms are not written explicitly in Eqs. (A4) and (A5) due to their similarity, and they do not alter the populations significantly due to the NA process being a time-zero effect. We describe the motion of the dynamic barrier potential as

$$U^{ac}_{G1}(t) = 2V^{ac}_{G1pk}\alpha_{G1}ft + \alpha_{G2}V_{G2}, \tag{A4}$$

where V^{ac}_{G1pk} is the peak-to-peak amplitude of V^{ac}_{G1}, which is 1.6 V; α_{G1} describes the coupling between $V^{ac}_{G1}(t)$ and $U^{ac}_{G1}(t)$, and α_{G2} describes the coupling between V_{G2} and $U_G(t)$; $\alpha_{G1} = 0.55$ is determined by examining the conductance in the 2D parameter range $V^{ac}_{G1}(t), V_{G2}$ [9]; and $\alpha_{G2} = 0.10$ is chosen by a fit of the low-frequency, low-temperature model result to the data. Neither of the latter values changes with frequency [9,30]. The QD potential rises as

$$U_G(t) = (\alpha_{G1-G}/\alpha_{G1})(U^{ac}_{G1}(t) - \alpha_{G2}V_{G2}) - E_c, \tag{A5}$$

where $\alpha_{G1-G} = g\alpha_{G1}/(1+g) = 0.5$ is the cross-coupling between $V^{ac}_{G1}(t)$ and $U_G(t)$; g is a measure of the coupling between the QD and $V^{ac}_{G1}(t)$, and we use $g = 10$ because of the high degree of cross-coupling [38]; $E_c = 16$ meV is the charging energy and is chosen in conjunction with $T_0 = 17$ K by the method detailed in Ref. [30]. Hence, $U_E(t)$ evolves as $U_G(t) + E$. In the absence of NA excitation (low frequencies), at $t = 0$, $P_{G,E}(0)$ is determined as a Fermi distribution between the two states $U_{G,E}(0)$:

$$P_G(0) = F(-E_c) \times F(-E), \quad P_E(0) = F(-E_c) \times F(E), \tag{A6}$$

and note that the probability of the QD and HE-state system being empty is $P_{zero} = 1 - F(-E_c)$. This is constructed such that only the QD can load. Then, $P_E(0)$ represents an initial thermal excitation taking place before the QD has completely isolated from the source.

[1] B. Kaestner and V. Kashcheyevs, Non-adiabatic quantized charge pumping with tunable-barrier quantum dots: A review of current progress, Rep. Prog. Phys. **78**, 103901 (2015).

[2] D. J. Reilly, Engineering the quantum-classical interface of solid-state qubits, npj Quantum Inf. **1**, 15011 (2015).

[3] L. P. Kouwenhoven, D. G. Austing, and S. Tarucha, Few-electron quantum dots, Rep. Prog. Phys. **64**, 701 (2001).

[4] C. L. Degen, F. Reinhard, and P. Cappellaro, Quantum sensing, Rev. Mod. Phys. **89**, 035002 (2017).

[5] J. D. Fletcher, N. Johnson, E. Locane, P. See, J. P. Griffiths, I. Farrer, D. A. Ritchie, P. W. Brouwer, V. Kashcheyevs, and M. Kataoka, Quantum tomography of solitary electrons, Nat. Commun. **10**, 5298 (2019).

[6] Y. Sherkunov, N. d'Ambrumenil, P. Samuelsson, and M. Büttiker, Optimal pumping of orbital entanglement with single particle emitters, Phys. Rev. B **85**, 081108(R) (2012).

[7] E. Bocquillon, F. D. Parmentier, C. Grenier, J.-M. Berroir, P. Degiovanni, D. C. Glattli, B. Plaçais, A. Cavanna, Y. Jin, and G. Fève, Electron quantum optics: Partitioning electrons one by one, Phys. Rev. Lett. **108**, 196803 (2012).

[8] E. Bocquillon, V. Freulon, J. M. Berroir, P. Degiovanni, B. Plaçais, A. Cavanna, Y. Jin, and G. Fève, Coherence and indistinguishability of single electrons emitted by independent sources, Science **339**, 1054 (2013).

[9] G. Yamahata, S. Ryu, N. Johnson, H.-S. Sim, A. Fujiwara, and M. Kataoka, Picosecond coherent electron motion in a silicon single-electron source, Nat. Nanotechnol. **14**, 1019 (2019).

[10] S. Bose and D. Home, Generic entanglement generation, quantum statistics, and complementarity, Phys. Rev. Lett. **88**, 050401 (2002).

[11] W. G. van der Wiel, S. De Franceschi, J. M. Elzerman, T. Fujisawa, S. Tarucha, and L. P. Kouwenhoven, Electron transport through double quantum dots, Rev. Mod. Phys. **75**, 1 (2002).

[12] S. P. Giblin, M. Kataoka, J. D. Fletcher, P. See, T. J. B. M. Janssen, J. P. Griffiths, G. A. C. Jones, I. Farrer, and D. A. Ritchie, Towards a quantum representation of the ampere using single electron pumps, Nat. Commun. **3**, 930 (2012).

[13] B. Kaestner, C. Leicht, V. Kashcheyevs, K. Pierz, U. Siegner, and H. W. Schumacher, Single-parameter quantized charge pumping in high magnetic fields, Appl. Phys. Lett. **94**, 012106 (2009).

[14] N. Johnson *et al.*, in preparation.

[15] S. Ryu, M. Kataoka, and H.-S. Sim, Ultrafast emission and detection of a single-electron Gaussian wave packet: A theoretical study, Phys. Rev. Lett. **117**, 146802 (2016).

[16] F. H. L. Koppens, C. Buizert, K. J. Tielrooij, I. T. Vink, K. C. Nowack, T. Meunier, L. P. Kouwenhoven, and L. M. K. Vandersypen, Driven coherent oscillations of a single electron spin in a quantum dot, Nature **442**, 766 (2006).

[17] M. F. Gonzalez-Zalba, S. N. Shevchenko, S. Barraud, J. R. Johansson, A. J. Ferguson, F. Nori, and A. C. Betz,

Gate-sensing coherent charge oscillations in a silicon field-effect transistor, Nano Lett. **16**, 1614 (2016).

[18] Z. Shi, C. B. Simmons, J. R. Prance, J. K. Gamble, T. S. Koh, Y.-P. Shim, X. Hu, D. E. Savage, M. G. Lagally, M. A. Eriksson, M. Friesen, and S. N. Coppersmith, Fast hybrid silicon double-quantum-dot qubit, Phys. Rev. Lett. **108**, 140503 (2012).

[19] Z. Cai, A. Siegel, and S. Benjamin, Looped pipelines enabling effective 3D qubit lattices in a strictly 2D device, PRX Quantum **4**, 020345 (2023).

[20] H. Edlbauer *et al.*, Semiconductor-based electron flying qubits: Review on recent progress accelerated by numerical modelling, EPJ Quantum Technol. **9**, 21 (2022).

[21] R. Xue, M. Beer, I. Seidler, S. Humpohl, J.-S. Tu, S. Trellenkamp, T. Struck, H. Bluhm, and L. R. Schreiber, Si/SiGe QuBus for single electron information-processing devices with memory and micron-scale connectivity function, Nat. Commun. **15**, 2296 (2024).

[22] V. Kashcheyevs and B. Kaestner, Universal decay cascade model for dynamic quantum dot initialization, Phys. Rev. Lett. **104**, 186805 (2010).

[23] M. Kataoka, J. D. Fletcher, P. See, S. P. Giblin, T. J. B. M. Janssen, J. P. Griffiths, G. A. C. Jones, I. Farrer, and D. A. Ritchie, Tunable nonadiabatic excitation in a single-electron quantum dot, Phys. Rev. Lett. **106**, 126801 (2011).

[24] S. P. Giblin, A. Fujiwara, G. Yamahata, M.-H. Bae, N. Kim, A. Rossi, M. Möttönen, and M. Kataoka, Evidence for universality of tunable-barrier electron pumps, Metrologia **56**, 044004 (2019).

[25] A. Fujiwara, N. M. Zimmerman, Y. Ono, and Y. Takahashi, Current quantization due to single-electron transfer in Si-wire charge-coupled devices, Appl. Phys. Lett. **84**, 1323 (2004).

[26] A. Fujiwara, K. Nishiguchi, and Y. Ono, Nanoampere charge pump by single-electron ratchet using silicon nanowire metal oxide-semiconductor field-effect transistor, Appl. Phys. Lett. **92**, 042102 (2008).

[27] A. Rossi, T. Tanttu, K. Y. Tan, I. Isakka, R. Zhao, K. W. Chan, G. C. Tettamanzi, S. Rogge, A. S. Dzurak, and M. Möttönen, An accurate single-electron pump based on a highly tunable silicon quantum dot, Nano Lett. **14**, 3405 (2014).

[28] G. Yamahata, S. P. Giblin, M. Kataoka, T. Karasawa, and A. Fujiwara, High-accuracy current generation in the nanoampere regime from a silicon single-trap electron pump, Sci. Rep. **7**, 45137 (2017).

[29] A. Fujiwara, Y. Takahashi, H. Namatsu, K. Kurihara, and K. Murase, Suppression of effects of parasitic metal-oxide-semiconductor field-effect transistors on Si single-electron transistors, Jpn. J. Appl. Phys. **37**, 3257 (1998).

[30] N. Johnson, G. Yamahata, and A. Fujiwara, Measurement of the curvature and height of the potential barrier for a dynamic quantum dot, Appl. Phys. Lett. **115**, 162103 (2019).

[31] T. Brandes and T. Vorrath, Adiabatic transfer of electrons in coupled quantum dots, Phys. Rev. B **66**, 075341 (2002).

[32] B. Kaestner, V. Kashcheyevs, G. Hein, K. Pierz, U. Siegner, and H. W. Schumacher, Robust single-parameter quantized charge pumping, Appl. Phys. Lett. **92**, 192106 (2008).

[33] G. Yamahata, S. P. Giblin, M. Kataoka, T. Karasawa, and A. Fujiwara, Gigahertz single-electron pumping in silicon with an accuracy better than 9.2 parts in 10^7, Appl. Phys. Lett. **109**, 013101 (2016).

[34] G. Yamahata, K. Nishiguchi, and A. Fujiwara, Accuracy evaluation and mechanism crossover of single-electron transfer in Si tunable-barrier turnstiles, Phys. Rev. B **89**, 165302 (2014).

[35] A. Fujiwara, G. Yamahata, and K. Nishiguchi, in *Nanoscale Silicon Devices* (CRC Press, Boca Raton, Florida, USA, 2016), Chap. 9.

[36] M. Dür, A. D. Gunther, D. Vasileska, and S. M. Goodnick, Acoustic phonon scattering in silicon quantum dots, Nanotechnology **10**, 142 (1999).

[37] A. Fujiwara *et al.*, in preparation.

[38] G. Yamahata, N. Johnson, and A. Fujiwara, Understanding the mechanism of tunable-barrier single-electron pumping: Mechanism crossover and optimal accuracy, Phys. Rev. B **103**, 245306 (2021).